ELSEVIER

doi:**10.1016/j.ultrasmedbio.2011.06.006**

● *Original Contribution*

AUTOMATIC ADAPTIVE PARAMETERIZATION IN LOCAL PHASE FEATURE-BASED BONE SEGMENTATION IN ULTRASOUND

ILKER HACIHALILOGLU,* RAFEEF ABUGHARBIEH,* ANTONY J. HODGSON,[†] and ROBERT N. ROHLING*[†]

*Department of Electrical and Computer Engineering, University of British Columbia, Vancouver, BC, Canada; and [†]Department of Mechanical Engineering, University of British Columbia, Vancouver, BC, Canada

Abstract—Intensity-invariant local phase features based on Log-Gabor filters have been recently shown to produce highly accurate localizations of bone surfaces from three-dimensional (3-D) ultrasound. A key challenge, however, remains in the proper selection of filter parameters, whose values have so far been chosen empirically and kept fixed for a given image. Since Log-Gabor filter responses widely change when varying the filter parameters, actual parameter selection can significantly affect the quality of extracted features. This article presents a novel method for contextual parameter selection that autonomously adapts to image content. Our technique automatically selects the scale, bandwidth and orientation parameters of Log-Gabor filters for optimizing local phase symmetry. The proposed approach incorporates principle curvature computed from the Hessian matrix and directional filter banks in a phase scale-space framework. Evaluations performed on carefully designed *in vitro* experiments demonstrate 35% improvement in accuracy of bone surface localization compared with empirically-set parameterization results. Results from a pilot *in vivo* study on human subjects, scanned in the operating room, show similar improvements. (E-mail: rafeef@ece.ubc.ca) © 2011 World Federation for Ultrasound in Medicine & Biology.

Key Words: Ultrasound, Local phase features, Principle curvature, Automatic parameter selection, Phase symmetry, Bone, Segmentation, Log-Gabor filters, Orthopaedic.

INTRODUCTION

Ultrasound (US) image feature extraction algorithms are strongly influenced by the quality of the acquired data. Characteristic artifacts, such as low signal-to-noise ratio and shadowing, significantly complicate image interpretation and automatic processing. Further complications arise due to image gray level variations within and across images. Recent advances in US technology, including advanced transducer design, increased spatial and temporal resolutions, real-time digital signal processing and miniaturization have led to a significant increase in the use of US in image-guided interventions. Examples include orthopaedics (Barrat et al. 2006, 2008; Beek et al. 2008; Penney et al. 2006), cardiology (Bosch et al. 2002; Boukerroui et al. 2001), breast oncology (Madabhushi et al. 2003) and prostate oncology (Pathak et al. 2000). US imaging has frequently been proposed

as a potentially valuable modality for use in orthopaedic applications as it can provide real-time imaging data without exposing either the patient or the surgical team to radiation. Current and proposed applications include identification of landmarks (*e.g.*, pelvic landmarks used to define the anterior pelvic plane in hip replacement surgery [Barrat et al. 2006; 2008]), registration of preoperative models (Barrat et al. 2008) and visualization of the quality of fracture reductions (Beek et al. 2008; Kryvanos 2002). In all of these situations, it is highly desirable to rapidly and automatically extract the relevant bone surface information from the B-mode US images because it is impractical to have the surgeon manually digitize points on US images during a live procedure. This has naturally led to an increased need for developing automatic image segmentation methods capable of localizing anatomical structures of interest with sufficient accuracy and efficiency without being affected by the typical US imaging artifacts.

In this article we focus on bone US imaging in the context of orthopaedic fracture surgeries. Our main interest is in bone fractures of the distal radius, which are responsible for about one sixth of all fractures seen

in emergency departments in the United States (Hanel et al. 2002; McMurtry et al. 1997), as well as fractures of the pelvis (Coppola and Coppola 2000).

Several researchers investigated the use of US in orthopaedic surgery. Tonetti et al. (2001) registered manually-digitized bone contour points from B-mode ultrasound images of a pelvis to their corresponding computed tomography (CT) datasets. In a different study on human cadavers, Barratt et al. (2006) manually segmented the pelvis and femur bone surfaces from US data and registered them to corresponding CT dataset. Despite the accurate results obtained in these studies, they suffered from major drawbacks including the significant time and effort needed for manual segmentation, as well as the large inter- and intra-user variability (Barratt et al. 2006; Beek et al. 2008). To overcome such limitations and to automate the bone surface extraction procedure, methods based on image intensity and local gradient information have been used (Daanen et al. 2004; Foroughi et al. 2007; Kowal et al. 2007; Kryvanos 2002). However, managing the sensitivity of intensity and gradient-based techniques to US artifacts, machine settings and algorithm parameters remains a serious challenge. In particular, small scale variations resulting from speckle must be addressed explicitly to reduce the incidence of false bone edge detection. Also, the dependence of bone appearance on the US beam direction increases the number of false and missed edges. To make segmentation more robust, methods were proposed for incorporating *a priori* bone appearance information into the segmentation framework (Daanen et al. 2004; Foroughi et al. 2007; Jain and Taylor 2004). However, fractured bone surfaces in orthopaedic surgery applications, as well as reduced bones secured with internal fixation devices, do not have a continuous smooth surface and often significantly violate prior assumptions regarding bone shape. Some groups have proposed methods combining segmentation techniques with multimodal registration of US and CT (Amin et al. 2003; Brendel et al. 2002; Ionescu et al. 1999). However, in orthopaedic surgery, CT is not routinely used for many types of fractures and is reserved for cases where the fracture is complex and the identification of the fractured parts has proven to be difficult with standard fluoroscopy. CT scanning of all fracture cases for the purpose of US segmentation would increase the associated costs and radiation exposure, which defeats one of the main advantages of employing US.

Intensity invariant local phase-based feature extraction has been shown to be promising for processing US images of soft tissue (Boukerroui et al. 2001; Cao et al. 2006; Grau and Noble 2005; Mulet-Parada and Noble 2000; Sanchez-Ortiz et al. 2000; Ye and Noble 2002) and, more recently, bone surfaces (Hacihaliloglu et al. 2006, 2009a). Although such phase-based techniques successfully extracted the desired image features, they remain sensitive to the underlying filter parameters used. Previous approaches totally relied on empirical selection of suitable filter parameters, which was performed by trial and error and ad hoc investigations of filter outputs on samples of US images depicting a certain anatomical area of interest (Hacihaliloglu et al. 2006, 2009a; Kovesi 1997; Mulet-Parada and Noble 2000). Once acceptable filter parameters were found, they were typically fixed for subsequent applications to new data. The difficulty in relating correct parameter choices to the properties of the image and image-processing task has thus inhibited more widespread use of phase-based techniques.

In this work (Preliminary results of this work appeared in Hacihaliloglu et al. (2009b), we present a novel method for automatic selection of the scale, bandwidth, orientation and angular bandwidth parameters in Log-Gabor filter-based phase symmetry (PS) in US images, specifically in the context of bone surface localization. Our proposed approach relies on contextual information obtained solely from image content by incorporating the principal curvature computed from the Hessian matrix and directional filter banks in a phase scale-space framework.

We present extensive validation studies using carefully designed *in vitro* experiments as well as an *in vivo* study of human subjects with distal radius fractures. We quantitatively demonstrate the utility of our parameter selection approach, its insensitivity to US artifacts when detecting bone boundaries and its superior performance in terms of surface localization accuracy.

METHODS AND MATERIALS

Review of Log-Gabor filter-based analysis of bone US

Previous work by our group (Hacihaliloglu et al. 2009a) presented a local phase-based method for extracting ridge-like features, similar to those that occur at soft tissue/bone interfaces, using a PS measure. In this article, we improve our approach by completely automating the parameter selection process. Our bone segmentation approach focuses on extraction of ridge-like features but could be extended to other feature types. A ridge can be thought of as a one-dimensional (1-D) curve representing an axis of local symmetry. It is well known that symmetric features can be extracted using local phase information (Kovesi 1997). Local phase of a 1-D signal can be obtained by convolving the signal with a pair of band-pass quadrature filters (an odd filter and an even filter). Using the two filters in quadrature enables the calculation of signal amplitude and phase at a particular scale (spatial frequency)

at a given spatial location. One choice of quadrature filters is the Log-Gabor filter, $R(\omega,\omega_0)$, which can be constructed with an arbitrary bandwidth. To obtain simultaneous localization of spatial and frequency information, analysis of the signal must be done over a narrow range (scale) of frequencies at different locations in the signal. This can be achieved by constructing a filter bank using a set of quadrature filters created from rescalings of the Log-Gabor filter.

This analysis can be extended into two dimensions (2-D) where a filter tuned to a particular orientation, ϕ_0, in the frequency domain (ω) is constructed by multiplying a radial Log-Gabor function, $R(\omega,\omega_0)$, with an angular Gaussian, ($G(\phi,\phi_0)$), tuned to ϕ_0:

$$PS(x,y) = \frac{\sum_r \sum_m \lfloor [|e_{rm}(x,y)| - |o_{rm}(x,y)|] - T_r \rfloor}{\sum_r \sum_m \sqrt{e_{rm}^2(x,y) + o_{rm}^2(x,y)} + \varepsilon} \qquad (2)$$

Where $[e_{rm}(x,y), o_{rm}(x,y)] = [real(F^{-1}(2DLG \times F(I(x,y)))), imag(F^{-1}(2DLG \times F(I(x,y))))]$. F and F^{-1} denote the forward and inverse Fourier transforms respectively and $I(x,y)$ is the B-mode US image. T_r is a noise threshold value calculated from the smallest scale filter response and ε is a small number included to avoid division by zero.

Proposed data-driven filter parameterization

The appropriate design of the Gabor filter bank relies on the proper selection of the set of its main parameters,

$$2DLG(\omega,\phi) = R(\omega,\omega_0) \times G(\phi,\phi_0) = \exp\left(-\frac{(\log^2(\omega/\omega_0))}{2(\log^2(\kappa/\omega_0))}\right) \times \exp\left(-\frac{(\phi-\phi_0)^2}{2\sigma_\phi^2}\right) \qquad (1)$$

Here, κ is the standard deviation of the filter in the radial direction, and ω_0 is the filter's center spatial frequency. The term κ/ω_0 is related to the bandwidth (β) of the filter with $\beta = -2(\log 2/2)^{(-0.5)}\log(\kappa/\omega_0)$ (Hacihaliloglu et al. 2009a).

The scaling of the radial Log-Gabor function is achieved by using different wavelengths that are based on multiples of a minimum wavelength, λ_{min}, which is a user-defined parameter. The relationship between the filter scale m, and the filter center frequency ω_0 is set as $\omega_0 = 1/(\lambda_{min} (\delta)^{m-1})$ where δ is a scaling factor defined for computing the center frequencies of successive filters. $\sigma_\phi = \Delta\phi/s$ defines the angular bandwidth $\Delta\Omega = 2\sigma_\phi(2\log 2)^{0.5}$ where $\Delta\phi$ is the angular separation between neighbouring orientations and is defined as $\Delta\phi = 180°/N_r$ and N_r denotes the total number of orientations used. The parameter s is the standard deviation of the Gaussian spreading function in the angular direction that describes the filter's angular selectivity. To obtain higher orientation selectivity, the angular function must become narrower. Steering of the filter is achieved by changing its angle (ϕ_0). In our previous work (Hacihaliloglu et al. 2009a), these filter parameters were empirically set by extensively investigating the Log-Gabor filter outputs on different US images of *in vivo* human distal radius and pelvis data. Designing a filter with two scales ($m = 2$) and six orientations ($N_r = 6$), with $\kappa/\omega_0 = 0.25$ and a min filter wavelength of $\lambda_{min} = 25$ pixels typically offered reasonable spectral coverage and orientation resolution and produced good bone surface localization in the presence of speckle. Using this 2-D Log-Gabor filter the 2-D PS measure is calculated as:

namely; bandwidth (β), scale (λ_{min}), angular bandwidth ($\Delta\Omega$) and orientation (ϕ_0). The combination of these various parameters directly affects the filter's ability to extract accurate local phase image features. In the following sections, we analyze the Log-Gabor filter response in detail and present a data-driven approach for contextual selection of these parameters. Our approach first optimizes the bandwidth according to image acquisition properties. We then optimize for the scale parameter based on a set of initial filter orientations extracted through analysis of bone surface orientation information from the B-mode US image. We finally optimize for the orientations and angular bandwidth parameters.

Filter bandwidth selection

The filter bandwidth in the radial direction ($\beta = -2 (2/\ln 2)^{0.5} \ln(\kappa/\omega_0)$) is related to both the spatial extent of the US speckle and the boundary responses in the image. We therefore first estimate the image speckle size by generating a set of images covering a range of depths acquired by the US transducer (in our experiments, the transducer's center ultrasound frequency = 7.5 MHz, image depth setting ranged between 1.9 cm and 7.2 cm). Since the grey level in the US images used in this study is compressed on a logarithmic scale, we first map the gray level to a linear scale using $I_L(x,y) = 10^{I(x,y)/51}$ where $I(x,y)$ is the decompressed grey level intensity of the pixel located at the image coordinates (x,y) (Smith et al. 2000). By analysing a region with fully developed speckle from each image in the set, we compute the autocorrelation of each region and extract the full-width at half-maximum (FWHM) value, which we then use as a measure of the

speckle size similar to (Wagner et al. 1983). Although the speckle size is known to vary spatially, the location of the bone surface can be at an arbitrary location, so the entire image was used to calculate speckle size. In practice, the bone reflection is typically near the focal field and the average speckle size calculated from the whole image is similar to the speckle size near the focal region. We, thus, compute the ratio, κ/ω_0, for each image using:

$$\kappa/\omega_0 = \exp\left(-\frac{1}{4}\sqrt{2\times ln(2)}\times FWHM\times r\right) \quad (3)$$

where r is the pixel size in mm. We average the κ/ω_0 ratio over the set of different B-mode US test images (25 images in our experiments). The resultant average is then set as the filter bandwidth. Note that selecting a bandwidth significantly greater than this value (*i.e.,* selecting a smaller value for κ/ω_0) will result in a filter that fails to separate small scale speckle features from larger scale boundary responses. On the other hand, selecting a significantly lower bandwidth will reduce the accuracy of the boundary detection and cause blurring of the detected bone boundary (Fig. 1).

Initial filter orientation selection

The orientation of the Log-Gabor filter is controlled by the angular Gaussian function ($G(\phi,\phi_0)$). During the calculation of the PS metric, the filter is directed at a number of orientations. Commonly, six orientations are employed to cover the entire angular range ($0°$–$150°$

with $30°$ increments), with the responses subsequently averaged (Hacihaliloglu et al. 2006, 2009a; Kovesi 1997; Mulet-Parada and Noble 2000). However, given the highly directional nature of ultrasound bone image data, integration of responses from all these different filter orientations in fact largely degrades the PS response due to the inclusion of many irrelevant filter orientations. Noting that the strongest ridge features appear when the filter orientation is perpendicular to the bone surface (Fig. 2), identifying and combining filter angles which produce strong responses will therefore likely enhance feature extraction.

Bone surfaces in B-mode US images typically appear as elongated line-like objects with a higher gray level value compared with the other image features. A similar observation applies to the corresponding PS images. Therefore, integration along a bony feature produces a higher intensity value than doing the integration along a non-bony feature. Using this simple fact, we employ the radon transform (RT) to detect the orientation of such line-like structures. To automatically define meaningful starting angles for our filter, we initially cluster the RT (obtained from the B-mode US image) image using k-means clustering (Fig. 3).

The projection angles corresponding to the peak values of the RT generally reflect the angles perpendicular to the high-intensity features, *i.e.*, the bone surfaces in our case. Those angles are therefore used for initializing the orientations of the Log-Gabor filter. During the identification of distal radius fractures in a clinical
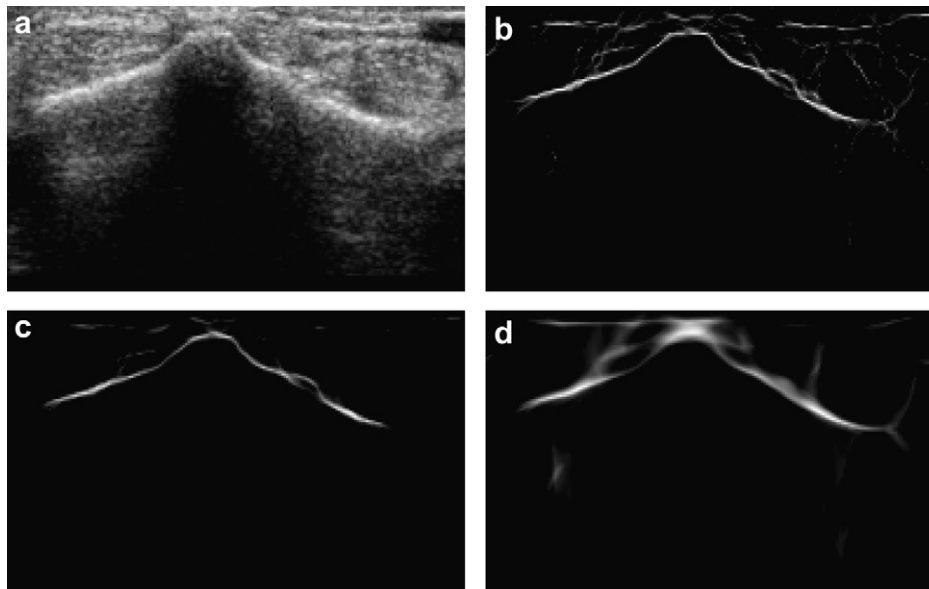

Fig. 1. Effect of filter bandwidth selection on local phase-based bone detection. (a) *In vivo* B-mode ultrasound (US) image of human distal radius. (b)–(d) Phase symmetry (PS) images obtained using κ/ω_0 values of 0.05, 0.24 and 0.55, respectively. (b) illustrates unintended speckle detection at high bandwidths, (d) illustrates bone boundary blurring at low bandwidths, while (c) reflects the effect of selecting an appropriate bandwidth where the PS captures continuous sections of the bone with little influence exhibited by soft-tissue interfaces and speckle.
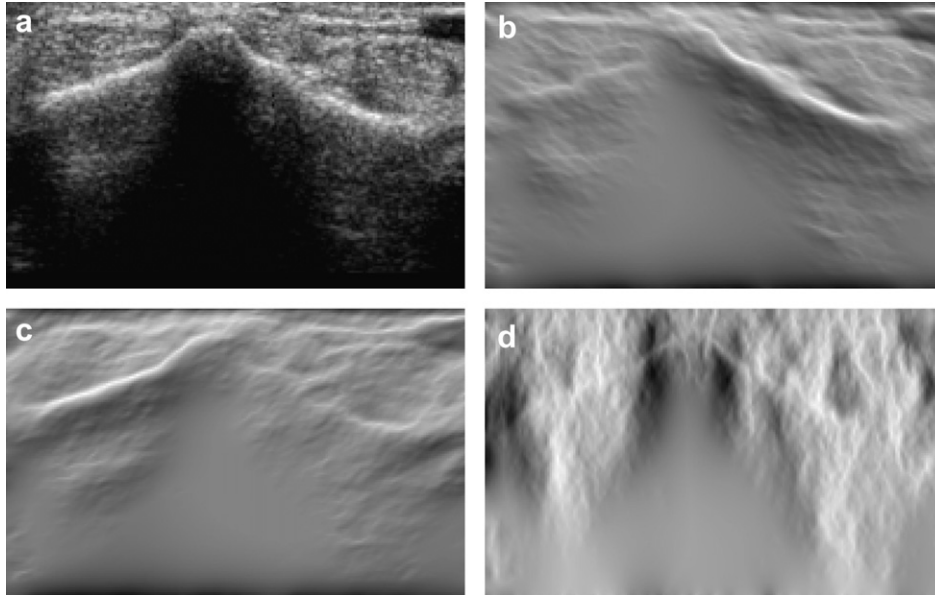
Fig. 2. Effects of filter orientation selection. (a) B-mode US of *in vivo* distal radius. (b) filter response at $\phi = 60°$. (c) Filter response at $\phi = 120°$. (d) Filter response at $\phi = 0°$. All images were produced at a fixed filter scale of $\lambda_{min} = 25$ and $\kappa/\omega_0 = 0.25$ degraded bone surface due to the inclusion of less informative orientations with weaker bone responses.

setting, the US transducer is positioned in dorsal, volar and radial sections. On the other hand, for pelvic ring factures the ultrasound images are obtained from maximally anterior left and right iliac spine points and, also, from the body of the pubis containing pubic tubercles to define the pelvic coordinate system. Investigating different *in vivo* scans obtained from these regions, we can see that bone surfaces produce either a curved (radius, femur) or a tilted response (pelvis). Therefore, constructing a filter with as little as three orientations is sufficient to cover the range of bone feature orientations that are present in the US images obtained from these regions.

Based on this analysis, three initial filter angles are selected, which we choose from the cluster corresponding to the peak values of the RT (Fig. 3c). Specifically, the mean value of the projection angles corresponding to the RT values in that chosen cluster and two additional angles set at ± 1 standard deviation within the threshold region are used. These three initial angles are used as the initial filter angle parameters during the calculation of the filter scale as explained in the next section.

Filter scale selection

Local image PS is computed by convolving the image with a number of scaled Log-Gabor filters. Each scaling is designed to pick out particular features of the image being analyzed with results typically integrated over multiple scales (in addition to multiple orientations) (Hacihaliloglu et al. 2009a). Since boundaries are extracted by analyzing the PS measure over a range of scales, correct scale selection is of major importance.

When using very small scales, the filters become highly sensitive to speckle. Selecting larger scales blurs the extracted bone features. Simply integrating different filter scales for PS calculations is typically inadequate as it results in PS images that either extract speckle or blurs the detected features (in our case bone boundaries), as demonstrated in Figure 4.

Line enhancing filters based on multiscale eigenvalue analysis of the Hessian matrix have been used to extract vessel-like structures in 2-D and 3-D medical images, *e.g.*, (Frangi et al. 1998). The scale selection approach we present in this article is inspired by this approach where we generate the Hessian matrix in (4):

$$H = \begin{bmatrix} L_{xx} & L_{xy} \\ L_{yx} & L_{yy} \end{bmatrix} , \quad L_{ab} = \frac{\partial^2 L}{\partial a \partial b} \quad (4)$$

where L is the image obtained by convolving the US image with the Log-Gabor filter at a particular scale. Here, the subscripts x and y represent spatial derivatives in the x and y directions, respectively. At this stage, the orientation of the Log-Gabor filter during the scale setting step is set to the initial filter angle calculated from the B-mode US image, as outlined in "*Initial Filter Orientation Selection*" section. We then calculate a ridge strength measure, $A_\gamma = t^{2\gamma}((L_{xx} - L_{yy})^2 + 4L_{xy}^2)$, which is the square of the γ normalized eigenvalue difference, with t being the scale of the filter ($t = \lambda_{min}$) (Lindeberg 1998) (Fig. 5). This metric in our context measures the "ridgeness content" of the image, since our main interest here is in localizing bone contours, which generally appear as ridges in US images. The optimal scale is, thus, defined
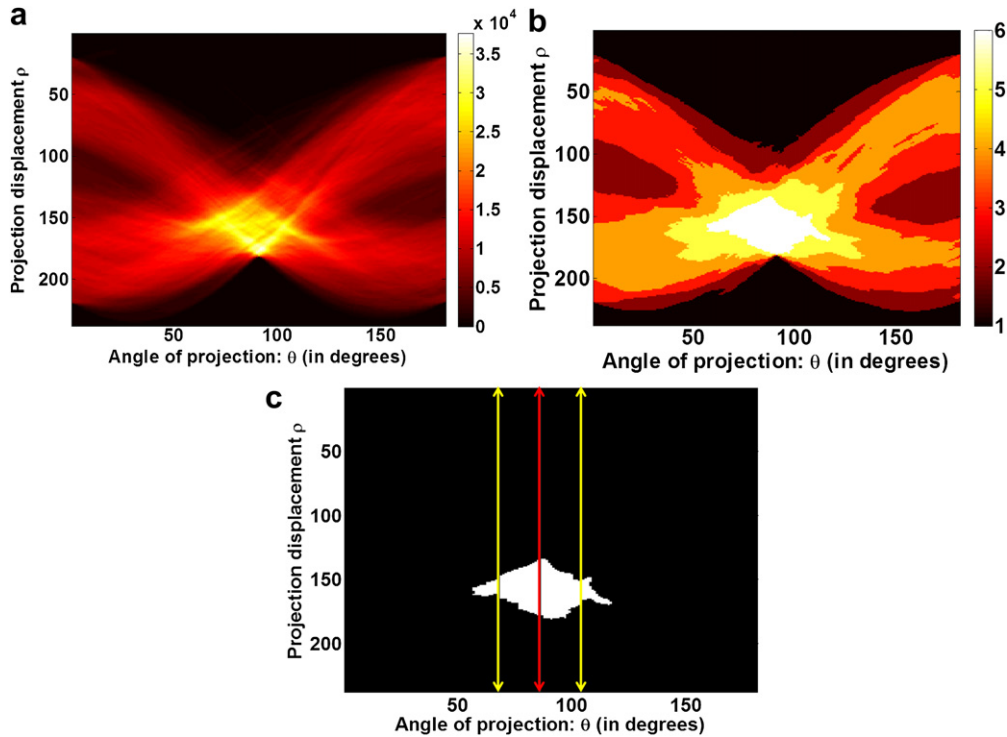
Fig. 3. Filter orientation selection step. (a) Radon transform (RT) of B-mode US image in Figure 2a, (b) k-mean clustered RT of (a), (c) the cluster corresponding to the highest RT values. The three initial angles deduced from this cluster are 68°, 86° and 104°. The arrows are pointing out to the location on the x-axis corresponding to the selected initial angle values. Red vertical arrow is the location of the mean value of the highest RT cluster (shown as white region in c) whereas yellow arrows are the location of the ± 1 standard deviation from the mean (left yellow arrow is the initial angle value corresponding to mean-standard deviation whereas the yellow arrow on the right is the initial angle values corresponding to mean + standard deviation).

as the one corresponding to the maximal ridgeness content in the Gabor filtered image. To define the optimum global filter scale, which highlights the most significant ridge content, we analyze the intensity distribution of A_γ over all possible scales (*e.g.*, ranging from 2 to 150 in our experiments). We then select the scale where the sum of the intensities achieves a maximum value as the optimal filter scale (Fig. 5d). This is based on the fact that at the optimal scale the response of the filter will produce a sharp ridge feature aligned with the bone surface, whereas significantly different scales will result either in detection of speckle or blurred bone surfaces which will reduce the intensity sum (Fig. 1a–c). This analysis is repeated for each orientation separately.

Filter orientation refinement

To select the final filter orientations, the RT is re-calculated for the ridge strength image A_γ as obtained using the scale calculated in "*Filter Scale Selection*" section. Figure 6 shows the calculated RT of the A_γ for the initial angle of 104° as an example. Noting that the RT has high intensity locations indicating the presence

of line-like structures in the image, the maximum value of the RT simply indicates the main orientation of the bone, since it has the strongest filter response, and is thus used to set the final filter orientation. Figure 6b shows an example where the angle corresponding to the peak occurs at 115°, hence, the initial angle set as per section "*initial filter orientation selection*" is corrected based on this new calculated angle. We note that this analysis is done for all the three initial filter angles obtained from section "*initial filter orientation selection*", but we only show example for one of the initial angles. Using more than three angles adds to the computational costs and did not improve the results significantly, so three are used in our experiments.

Filter angular bandwidth selection

The angular bandwidth parameter, $\sigma_\varnothing$, corresponds to the standard deviation of the Gaussian spreading function in the angular direction and describes the filter's angular selectivity. Investigating the example in Figure 7, we can see that large angular bandwidths make the Log-Gabor filter act as a smoothing filter, without being sensitive to any orientation. On the other
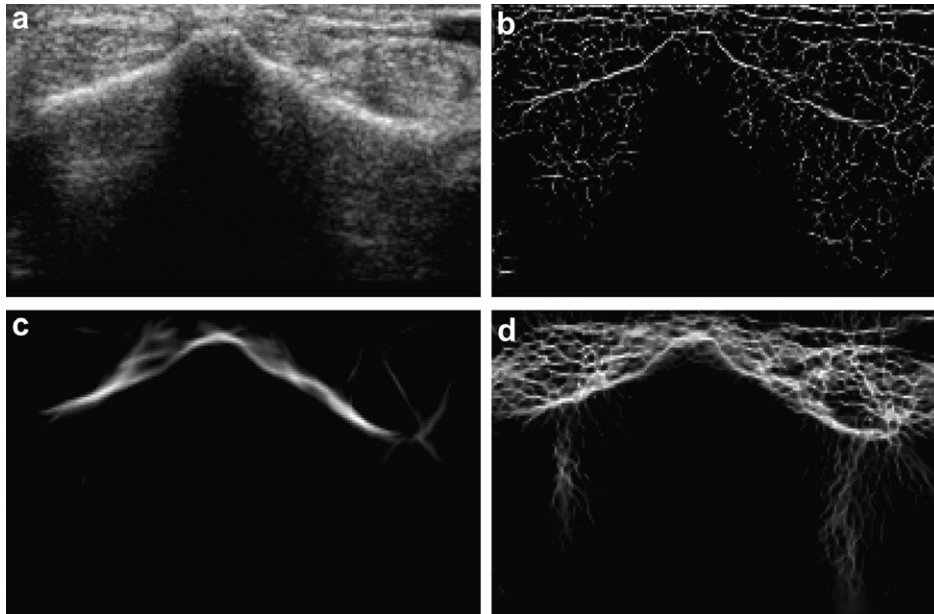
Fig. 4. Effects of filter scale selection. (a) Original B-mode US image of an *in vivo* distal radius. (b) Phase symmetry (PS) obtained using a scale value of $\lambda_{min} = 2$. (c) PS obtained using a scale value of $\lambda_{min} = 88$. (d) PS obtained by combining the results of both scales (2 and 88).

hand, for small angular bandwidths, the filter acts like a line detector degrading the curvature of the bone surface as it becomes less sensitive to curvature. This makes the extracted features look like short line segments when the true surface is curved. Therefore, using the same analysis we used in our filter scale selection process would not be suitable to set σ_φ, since the intensity distribution of A_γ over all possible angular bandwidths will give a peak at very large angular bandwidths. An example for his

situation is given in Figure 7 where selecting the peak value of the angular bandwidth vs. the sum of intensity values of A_γ corresponds to a filter response shown in Figure 7a.

We, thus, analyze the kurtosis of the RT of A_γ over the values of angular bandwidth. Higher kurtosis means more of the variance is due to infrequent extreme deviations (*i.e.*, an A_γ image with uniform black background with sharp high-intensity bone boundary), opposed to
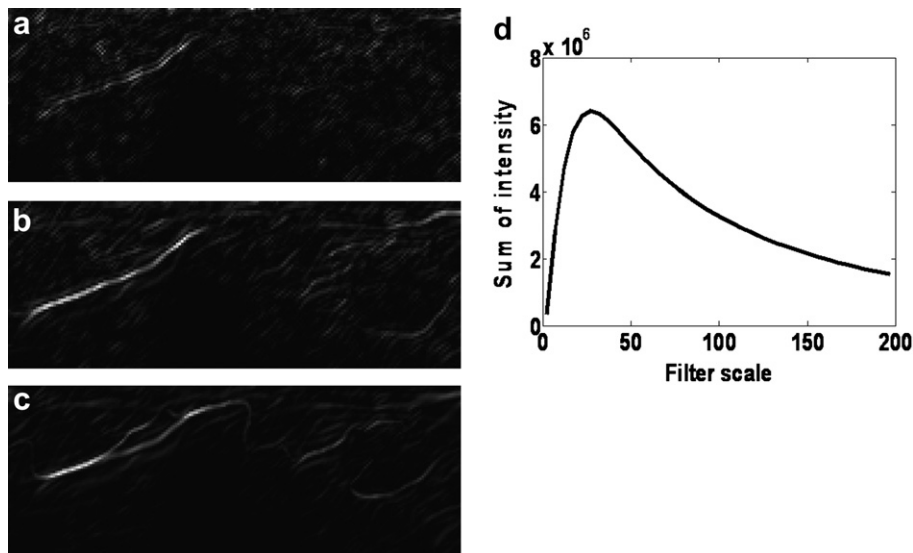

Fig. 5. Effects of filter bandwidth selection. A_γ ridge strength obtained from a B-mode ultrasound (US) image in Figure 2a for a fixed filter orientation (140°) and scale (a) $\lambda_{min} = 10$, (b) $\lambda_{min} = 35$ and (c) $\lambda_{min} = 140$. Investigating (a)–(c) we see that the bone ridge content in (b) is the strongest and the most continuous. (d) Filter scale vs. sum of intensity values of A_γ.
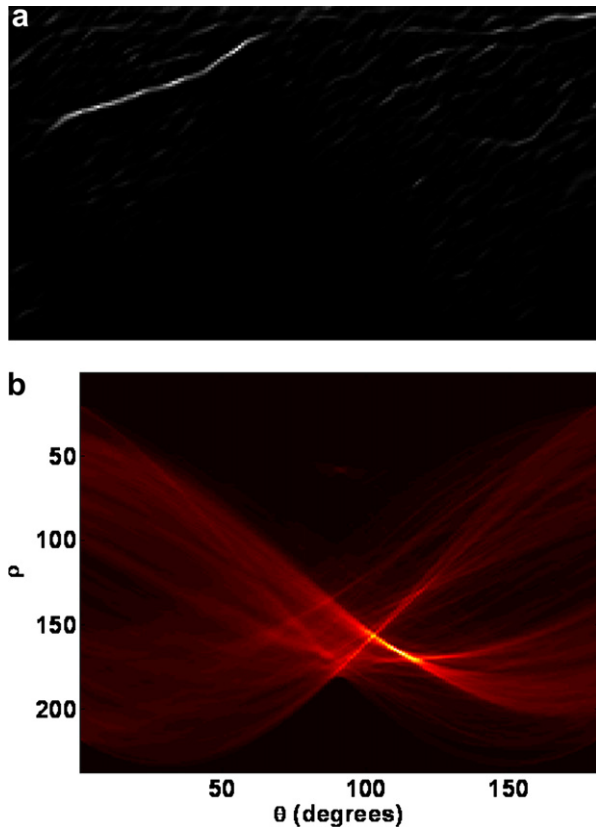
Fig. 6. Filter orientation selection. (a): A_γ obtained using the initial filter angle (a) $\phi = 104°$ which is calculated from the radon transform (RT) of the B-mode image, (b) RT of (a) showing new peak at 115°, respectively. The initial orientation of the filter is thus fine-tuned to 115°. This analysis is repeated for the other two initial filter angles as well.

frequent modestly-sized deviations (*i.e.*, an A_γ image with uniform black background degraded with speckle/ soft tissue interfaces or short line segments with different intensity values). We then select the bandwidth as that corresponding to the peak kurtosis value (Fig. 8b). During this stage, the A_γ images are obtained using the optimum filter scale as calculated in "*filter scale selection*" section.

Experimental set-up for quantitative validation

We constructed a phantom for validation purposes which comprised an *ex vivo* bovine femur specimen inside an open-topped Plexiglas cylindrical tube (The bovine specimen was obtained through a certified butcher following guidelines and notification of the UBC Animal Care and Biosafety Committee) (Fig. 9). Twenty-eight markers (1 mm diameter steel balls) were added to the phantom with fourteen beads placed on each side of the bone (longitudinally) and spaced at equal axial intervals over a distance of 75 mm. We obtained 3-D US scans of this phantom with each volume containing 16 fiducials (eight on each side) spanning a region of 37.8 mm. To hold the specimen and fiducials in place during the
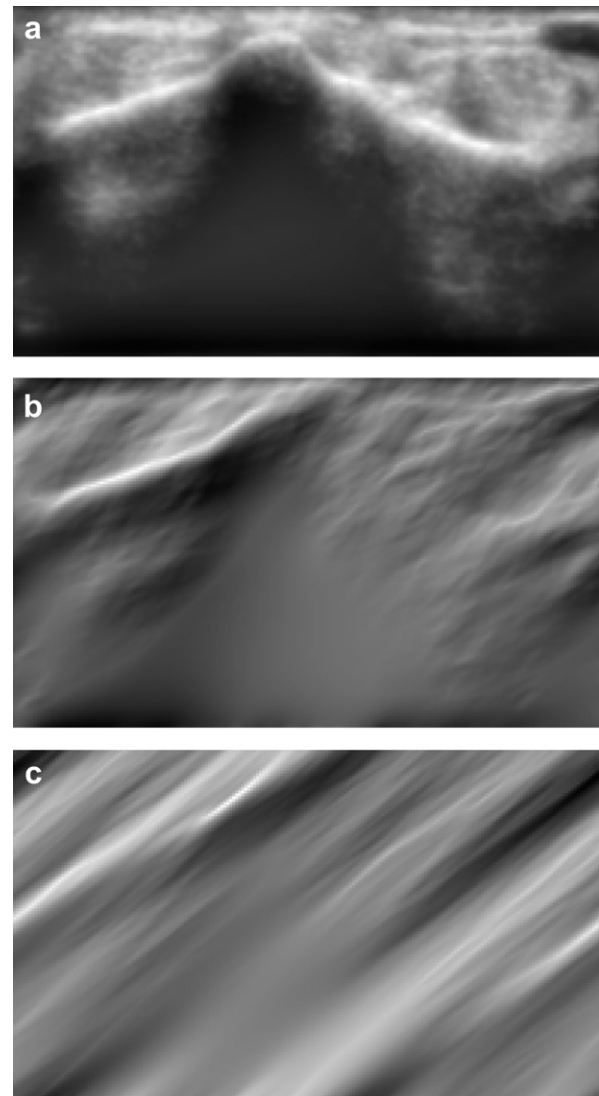

Fig. 7. Effect of varying angular bandwidth on the Log-Gabor filter output for filter orientation 115°. (a) $\sigma_\phi = 120°$, (b) $\sigma_\phi = 30°$ and (c) $\sigma_\phi = 7.5°$.

scanning procedures, the tube was filled with a firm gel (Super Soft Plastic; M-F Manufacturing, Fort Worth, TX, USA). The difference in the speed of sound in soft tissue (est. 1540m/s) and gel (est. 1340 m/s) during the image reconstruction process was compensated to improve the accuracy of alignment of the ultrasound and CT.

The constructed phantom was then scanned in an Xtreme CT machine with isometric 0.25 mm voxels. US scanning was performed using a 3-D GE Voluson 730 Expert system (GE Healthcare, Waukesha, WI) with a 3-D RSP5-12 probe. The reconstructed US volumes were 199 × 119 × 50 voxels (lateral × axial × elevational) with an isotropic voxel size of 0.19 mm. The US data was resampled to match the resolution of the CT image. Also, a fiducial-based rigid-body registration was applied to align the 3-D CT and 3D US volumes.
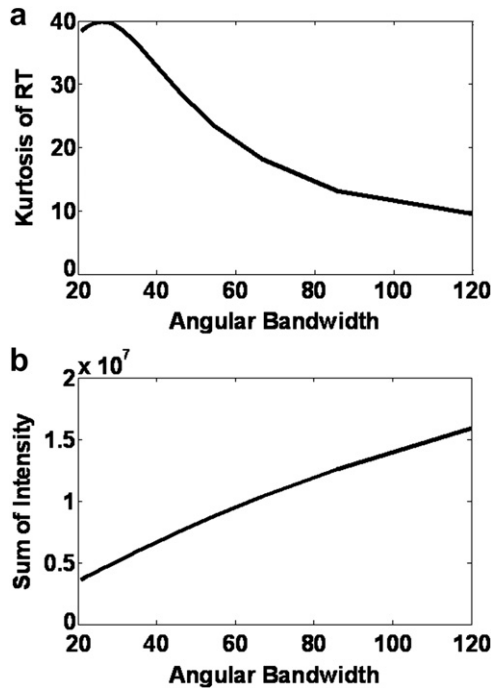
Fig. 8. Angular bandwidth selection step. (a) Filter angular bandwidth vs. sum of intensity values of A_γ. (b) Filter angular bandwidth vs. kurtosis of radon transform (RT) obtained from calculating the RT of A_γ.
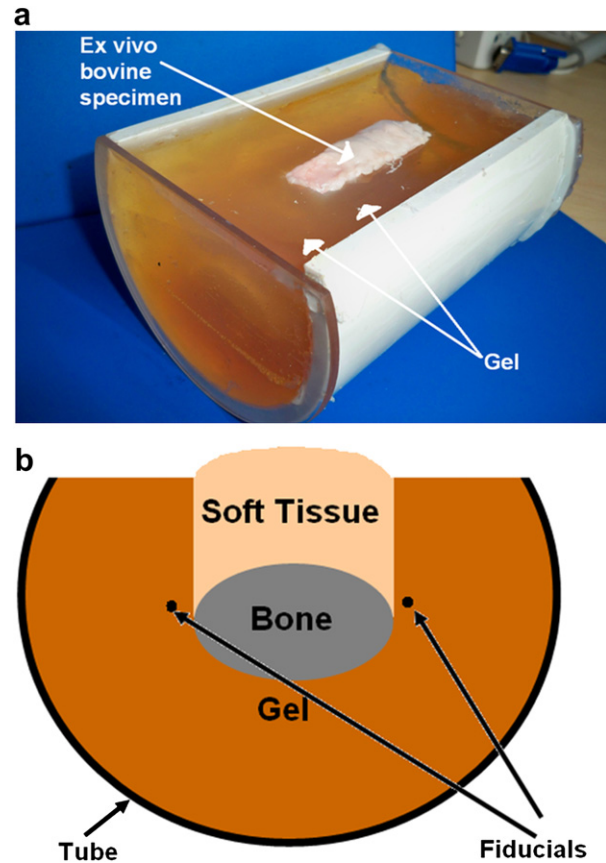

Fig. 9. Experimental set-up used for our quantitative validation. (a) Our constructed phantom comprised of an *ex vivo* bovine femur specimen inside an open-topped Plexiglas cylindrical tube filled with polyvinyl chloride gel. (b) Diagram depicting a 2-D axial cut of the constructed phantom showing the fiducials inserted into the gel.

Following registration, bone surfaces were extracted from CT scan using a simple thresholding operation to establish a 'gold standard' bone surface. Bone surfaces were then extracted from the 3-D US volume by processing each individual slice using our proposed PS features, both with (proposed method) and without (Hacihaliloglu et al. 2009a) parameters being optimized for comparison. To compare the gold standard surface (obtained from the CT data) to the US-extracted surface obtained using PS method, a signed distance map was computed around the bone surface contour extracted from the CT image. We then transformed each non-zero value in the phase-processed US image to its corresponding location in the CT image and identified the signed distance value associated with that location. This produced a set of intensity/distance pairs. High- intensity values confined to a zone near zero distance would indicate an accurately located surface. Our surface matching error was hence defined by the average signed distance values corresponding to the maximum phase intensity value along each vertical column of the 2-D PS images. This surface localization accuracy assessment was repeated for 15 different volumes obtained from the same specimen by processing each 2-D slice of the 3-D US volume and averaging the results.

We have also performed an exhaustive search for parameter selection to compare the localization accuracy achieved using the exhaustive search parameters with the accuracy found by using the proposed method. For the exhaustive search, PS images were extracted using all the possible parameter combinations and calculating the previously explained signed distance error metric. The optimum parameters were chosen as the ones that gave the lowest mean error.

Finally, to show that the proposed method is less sensitive to typical US artifacts and soft tissue interfaces, we also calculated the signed distance values corresponding to all PS intensity values rather than the maximum PS intensity in the vertical direction as done for surface localization accuracy assessment. This analysis was again repeated by processing each 2-D slice of the 3-D US volume and averaging the results. The method was implemented in MATLAB (The Mathworks Inc., Natick, MA, USA).

Clinical study

The patients were presented to the emergency department with right wrist pain. The fracture was

identified as a distal dorsal radius fracture. During the scanning, US coupling gel was placed on the skin over the dorsal, volar and radial sections. The patient scans were obtained after obtaining the ethical approval from UBC ethics board and obtaining signed consent of the patient. In total, 15 different US volumes for each patient were acquired. The gold standard comparison was provided by the 3-D surfaces extracted from the preoperative CT scans. The analysis was done by assessing the "fitness" of US derived surfaces to the gold standard which was achieved using the same procedure explained in previous section where a phantom set-up was used. US image was matched to the CT surface by matching selected anatomical landmarks (note: in previous *ex vivo* bovine study, we used implanted fiducials to perform the registration, but fiducials could not be used in this clinical study) and computing the rigid

body transformation. This registration procedure was repeated 10 times to compensate for the error that might be introduced during the anatomical landmark selection procedure.

Qualitative evaluation

We performed several qualitative evaluation tests using *in vivo* scans of a human distal radius and pelvis. We also demonstrate the effectiveness of the proposed method in extracting bone surfaces from US scans obtained during the clinical study.

RESULTS AND DISCUSSION

Quantitative results

The distribution of intensity values with their corresponding signed distance values obtained from one
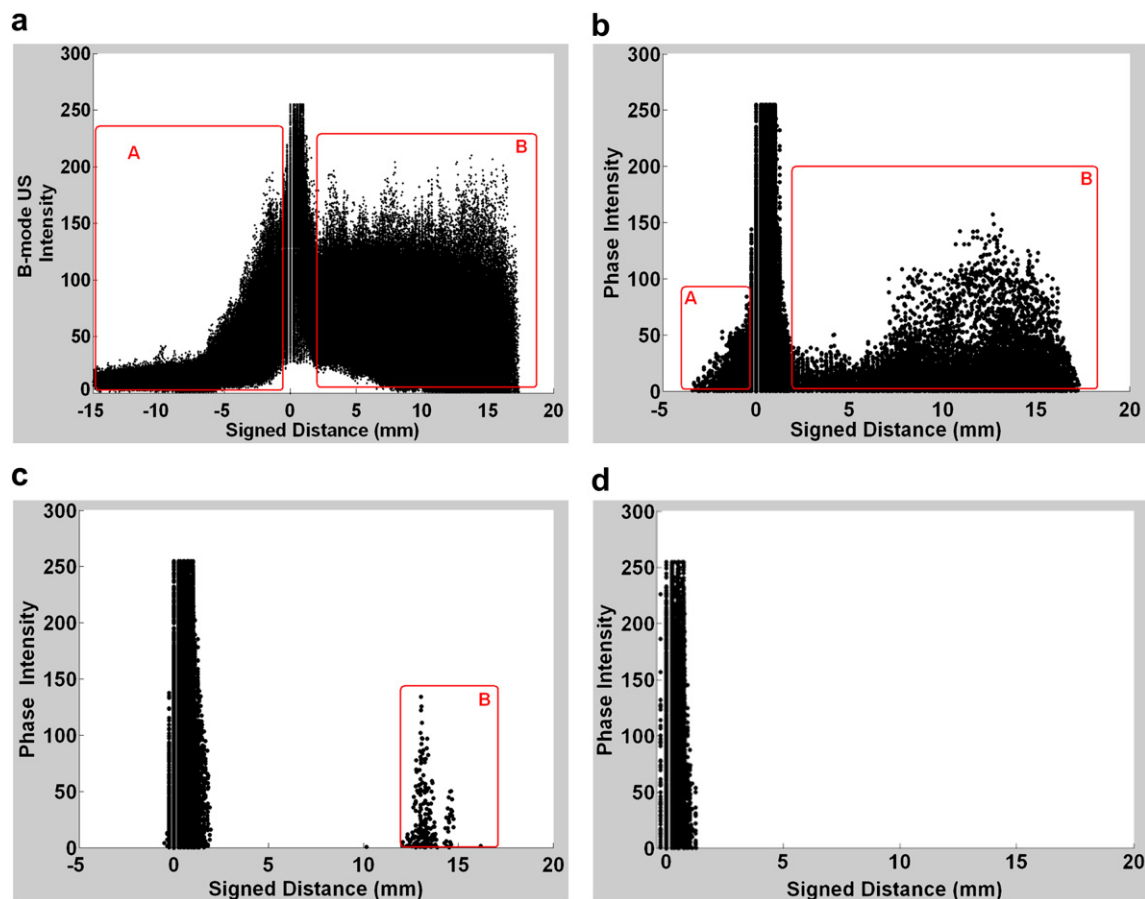

Fig. 10. Signed distance plots obtained from our quantitative validation experiment. (a) Signed distance (mm) vs. B-mode US image intensity. (b) Signed distance (mm) vs. phase intensity obtained from phase symmetry method with the best empirically set parameters using two scales. (c) Signed distance (mm) vs. phase intensity obtained from our proposed optimized parameter phase symmetry method. (d) Signed distance (mm) vs. phase intensity obtained from phase symmetry method using the exhaustive search parameters. Signed distance/intensity pairs inside the red rectangular boxes B reflect features corresponding to soft tissue interface or speckle noise. Signed distance/intensity pairs inside the red rectangular boxes A are features corresponding to shadowing artefact, speckle noise or thick bone response. Comparing these rectangles we can clearly see that with the proposed parameter optimization algorithm, the phase symmetry (PS) method becomes less sensitive to typical US artifacts.

Table 1. Quantitative results for bone surface localization accuracy assessment comparing empirical phase symmetry (PS) and exhaustive search PS with the proposed parameter tuned PS

| | Empirical PS | | | | Optimized PS | | Exhaustive search PS | |
| | One scale | | Two scales | | | | | |
Volume	Mean (mm)	STD (mm)	Mean (mm)	STD (mm)	Mean (mm)	STD (mm)	Mean (mm)	STD (mm)
1	1.67	3.91	3.32	4.70	0.77	2.17	1.54	2.88
2	2.03	4.56	3.87	5.21	1.98	4.21	0.55	1.81
3	2.54	4.91	3.46	5.48	0.91	2.74	0.67	1.85
4	1.84	4.12	3.19	4.74	1.2	3.15	1.19	3.49
5	3.1	4.17	4.20	4.85	2.44	3.47	1.02	2.31
6	3.07	4.60	4.28	5.09	2.6	4.11	0.35	1.65
7	2.62	3.95	3.85	4.97	2.35	3.91	0.37	0.47
8	2.52	4.48	4.49	5.30	2.85	4.88	3.42	5.23
9	2.33	4.06	3.74	5.03	2.26	3.94	0.36	0.46
10	2.03	4.05	3.07	4.84	1.7	3.5	0.69	2.4
11	2.13	4.09	3.39	4.98	2.61	4.43	0.81	2.50
12	1.78	4.26	2.71	4.72	1.54	3.66	2.03	4.55
13	0.95	4.01	2.84	4.94	0.22	2.18	0.50	3.44
14	2.65	4.70	4.29	5.32	3.97	5.07	3.36	5.28
15	0.97	4.07	2.92	4.98	0.23	2.50	0.57	3.62
Average	2.14	4.26	3.58	5.01	1.84	3.59	1.16	2.79

STD = standard deviation.
The results represent the average signed distance values that correspond to all phase intensity values of a 3-D US volume.

B-mode US image volume by processing each individual 2-D slice are shown in Figure 10. The figure also shows the corresponding results obtained from PS images calculated using the best empirically-set parameters and the PS image calculated using the proposed parameter optimized approach. Investigating these figures we can see that in both of the PS images, the concentration of the intensity values away from the zero signed distance value is much less compared with the B-mode US image gray level value distribution, which highlights the ability of the PS method in extracting bone surfaces without being affected by the US image artifacts. It can be easily noted how the PS obtained using the optimized parameters is much less sensitive to typical US artifacts or soft tissue interfaces compared with the PS obtained using the empirically-set parameters. Figure 10d shows the phase

Table 2. Quantitative results for bone surface localization accuracy assessment comparing empirical phase symmetry (PS) and exhaustive search PS with the proposed parameter tuned PS

| | EPS | | | | OPS | | ESPS | |
| | One scale | | Two scales | | | | | |
Volume	Mean (mm)	STD (mm)	Mean (mm)	STD (mm)	Mean (mm)	STD (mm)	Mean (mm)	STD (mm)
1	0.83	1.81	0.79	1.79	0.67	1.14	0.53	1.19
2	0.75	2.23	0.66	1.89	0.51	1.42	0.21	0.20
3	1.25	2.92	0.96	2.34	0.65	1.35	0.51	1.49
4	0.65	1.69	0.63	1.87	0.50	1.45	0.14	1.38
5	0.69	1.26	0.76	1.28	0.62	0.34	0.55	0.92
6	0.25	0.54	0.31	0.90	0.30	0.64	0.27	0.65
7	0.57	0.50	0.60	0.53	0.59	0.54	0.41	0.24
8	0.83	1.47	0.47	0.96	0.40	0.28	0.30	1.30
9	0.57	0.95	0.58	0.62	0.44	0.27	0.38	0.25
10	0.19	0.95	0.15	0.52	0.14	0.35	0.05	0.69
11	0.29	0.96	0.28	0.53	0.27	0.55	0.12	0.61
12	0.96	2.31	0.76	1.84	0.66	1.35	0.51	1.75
13	−0.35	1.39	−0.46	0.59	−0.40	0.15	−0.20	1.99
14	0.69	1.64	0.15	0.82	0.12	0.65	0.07	1.18
15	−0.40	1.38	−0.46	0.97	−0.50	0.17	−0.18	2.18
Average	0.51	1.46	0.41	1.16	0.33	0.71	0.24	1.06

EPS = empirical phase symmetry; ESPS = exhaustive search phase symmetry; OPS = optimized phase symmetry; STD = standard deviation.
The results represent the average signed distance values corresponding to the maximum phase intensity value along each vertical column of a 3D US volume.

Table 3. Quantitative results obtained from the clinical study

	Clinical study 1			Clinical study 2			Clinical study 3		
	EPS	OPS	ESPS	EPS	OPS	ESPS	EPS	OPS	ESPS
Average mean error (mm)	0.77	0.33	0.31	0.94	0.46	0.38	0.47	0.33	0.35
STD (mm)	1.10	0.52	0.59	1.45	0.55	0.74	1.39	0.88	1.41

EPS = empirical phase symmetry; ESPS = exhaustive search phase symmetry; OPS = optimized phase symmetry; STD = standard deviation.

intensity signed distance plot obtained from the exhaustive search method. Comparing this plot with the one obtained using the proposed method (Fig. 10c), we can see that the distribution of intensity values are really close

to the exhaustive search method which took about one day to compute. The results obtained from calculating the average signed distance values where all the PS intensity values were used are given in Table 1. Investigating
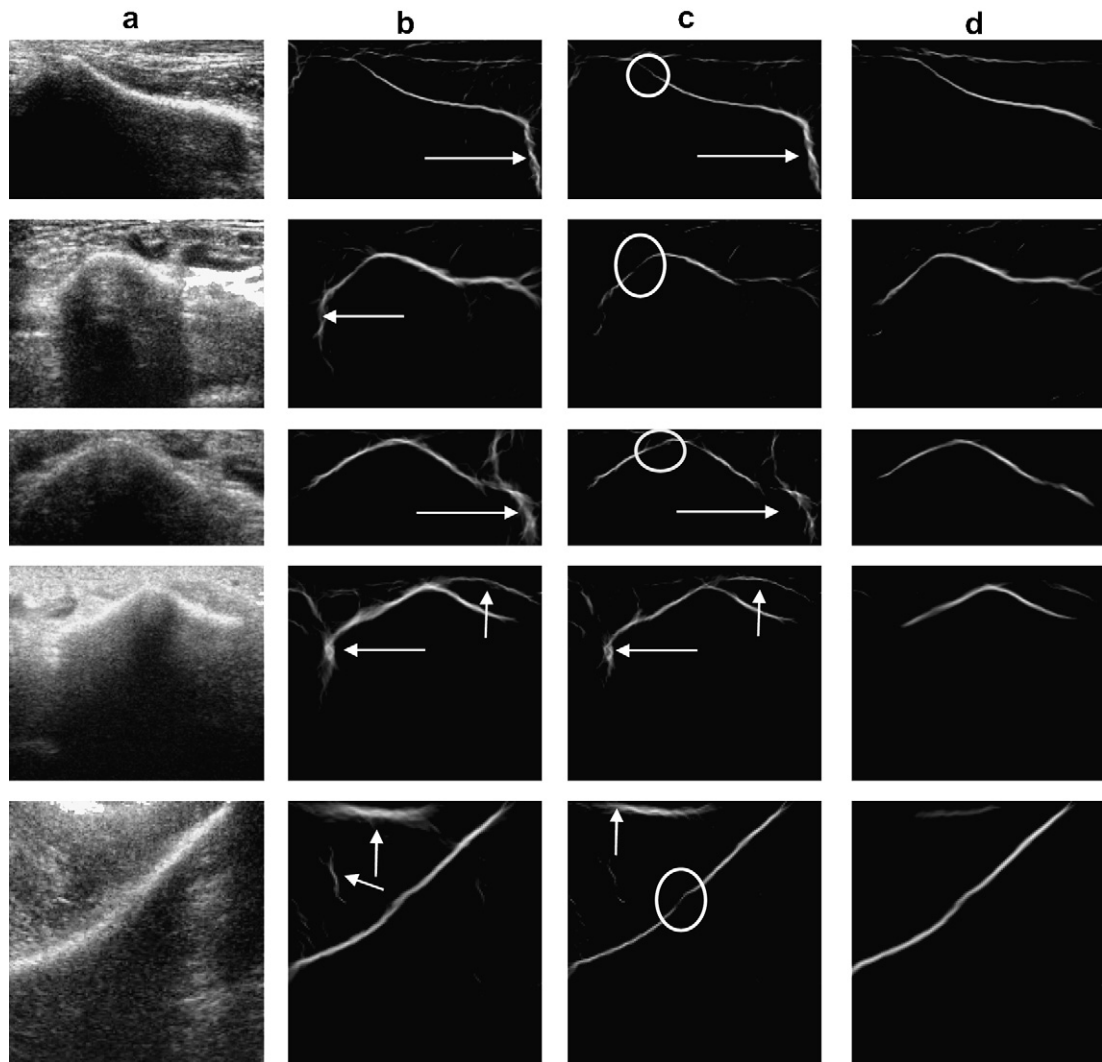

Fig. 11. Qualitative results on human *in vivo* data. (a) B-mode US image of distal radius (rows 1–4) and pelvis (row 5) areas. Imaging depth of the US machine was 3.5, 3.5, 1.9, 4.5 and 4.9 cm, respectively. (b) Nonoptimized phase symmetry (PS) images using two different filter scales (25 and 75). (c) Non-optimized PS images using one scale only (25). (d) PS images obtained using the proposed optimized parameters. White arrows point out some extracted phase features that are not bone surfaces due to combining orientations that are not perpendicular to the bone surface during the calculation of PS. The white circles highlights example locations of a degraded bone surface due to the inclusion of less informative orientations with weaker bone responses.

the results we can see that using the parameters derived from the image domain makes the Log-Gabor filter less sensitive to typical US artifacts (Table 1).

The average surface matching mean error was 0.51 mm (STD: 1.46 mm) with the best empirically-set parameters compared with 0.33 mm (STD: 0.71 mm) for our proposed automatically-set parameters (Table 2). Choosing two scales for the empirical method decreases the surface matching mean error to 0.41 mm (STD:

1.16 mm) but introduces more outlier points away from the zero signed distance indicating an increase in the detection of US artifacts (Table 1). The surface matching error with the best parameters from exhaustive search was 0.24 mm (STD: 1.06 mm).

Investigating Tables 1 and 2, we can see that the exhaustive search parameters achieve slightly better localization results than the proposed parameter selection method, but it should be noted that an
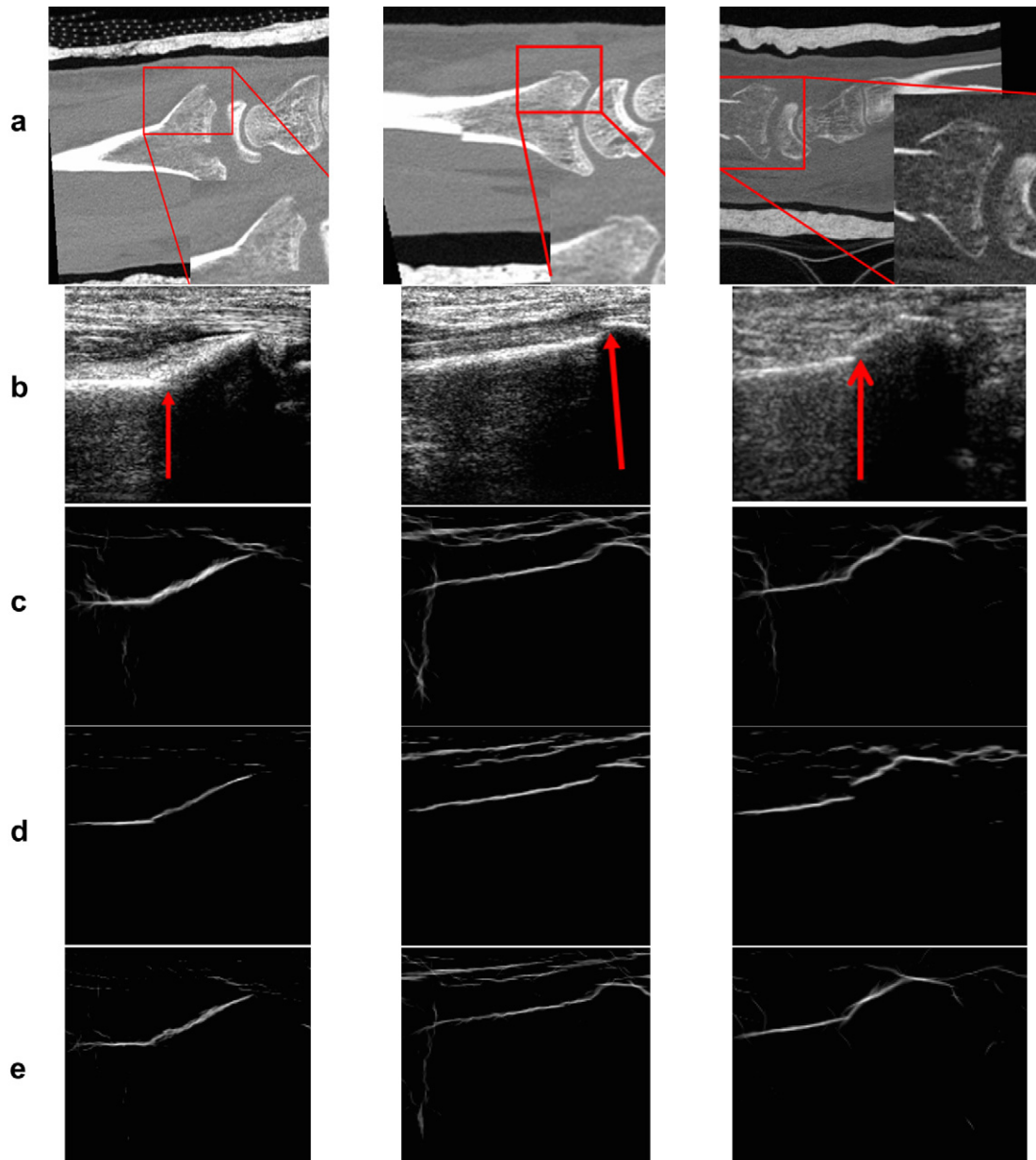

Fig. 12. Qualitative results from three clinical studies where the scanned area involved a distal radius fracture: one where the scanned area involved a distal radius fracture. (a) 2-D sagittal CT slice where the zoomed in version shows a clear fracture. (b) B-mode US image red arrow points out to the location of fracture, phase symmetry (PS) image obtained using empirical filter parameters. (c) PS image obtained using the filter parameters obtained from the proposed framework. (d) PS image using filter parameters obtained from exhaustive search procedure.

exhaustive search required 24 h to computer per image, compared with 6 s with the proposed method. It is, therefore, impractical to use an exhaustive search or even an iterative search for the optimal parameters in a clinical setting.

Clinical study results

Quantitative surface matching results are given in Table 3. The proposed method for optimizing the filter parameters results in an improvement on the surface localization accuracy.

Qualitative results

Figure 11 shows a qualitative comparison of PS images of an *in vivo* human distal radius and pelvis obtained with the proposed optimized Gabor filter parameters and contrasted to the best values we could empirically set. Note how the local phase images obtained empirically using two scales extracted more US artifacts and resulted in a thicker bone boundary due the unsuitable scale combination. Moreover, integrating the zero angle as one of the filter orientations caused the detection of unwanted features on the sides of the bone surface (Fig. 11, white arrows). Decreasing the filter scale to 1 in the empirical case caused gaps in the extracted bone surfaces (Fig. 11, white circles). Our surface results on the other hand, which used optimized filter parameters, were consistently sharper with reduced unwanted features on the bone sides and with no gaps in the detected surfaces. Finally investigating Figure 12, we can clearly see the importance of filter parameter selection on the clinical data as well. The local phase symmetry method with the optimized filter parameters is less sensitive to typical US artifacts and extracts sharper bone boundaries. Specifically, investigating the results from columns two and three, we can see that the gap between the fractured fragments is visualized better using the optimized filter parameters.

We believe that this filter bandwidth, scale and orientation adaptation approach addresses the key weaknesses of the previously published local phase based image enhancement methods (Hacihaliloglu et al. 2009a). In particular, the combination of automatic scale selection method with a simple orientation optimization module was shown to produce qualitatively and quantitatively improved results. It should be noted that the previous local phase-based feature extraction algorithms (Hacihaliloglu et al. 2009a) are likely to enhance speckle regions and soft tissue interfaces as well as bone surfaces since they do not provide and explicit mechanism for distinguishing between these features, whereas the proposed data driven approach handles this situation by means of a "ridgeness" measure for automatic scale selection and orientation optimization with RT.

Qualitative results obtained from *in vivo* and clinical scans demonstrated the critical importance of selecting the correct filter parameters in local phase based US processing. Quantitative results were also presented on a specially constructed bone phantom where the gold standard surface of the bone was established through CT imaging. An improvement of close to 0.18 mm in bone localization accuracy was observed. Furthermore, our adaptive parameter selection approach produces close to a 50% decrease in the variability and in the reduction of worst case scenario (*i.e.*, the standard deviation of the bone surface localization error for the proposed method [0.71 mm] is almost half of the empirical PS [1.46 mm] method) compared with empirical and exhaustive search methods. In US based computer assisted orthopaedic surgery (CAOS) systems, inaccuracies may arise from various sources such as US-CT registration, tracking of surgical instruments and localization of the surgical tool tips. Therefore, an improvement in bone surface extraction from US data plays an important role in all US based CAOS systems, which will in turn improve the total accuracy of the system that should be generally between 2 and 4 mm (Phillips 2007).

CONCLUSIONS

Though local image phase information has been successfully applied for extracting US image features, none of the prior studies investigated the effects of parameter setting on the extracted features nor provided guidelines on how proper selection could be achieved. Some authors left this as an open question for future development, while others tried to address it in an ad hoc manner, by investigating the filter outputs on samples of US imaged depicting a certain anatomical area of interest. In this article, we proposed a novel approach for automatic data-driven selection of the scale, bandwidth and orientation of Log-Gabor filters for calculating phase based features in bone US.

To determine the filter bandwidth, US images with fully developed speckle were analyzed and the image speckle size was measured by calculating the autocorrelation function. For scale selection, we used a "ridgeness content" measure obtained from the Hessian matrix eigenvalues. This measure was adopted since a line profile across a bone surface in an US response typically depicts a ridge-like rather than a step or ramp-like edge at the bone boundaries (Hacihaliloglu et al. 2009a). This metric could be changed to a step edge response, which is a common feature in echocardiography US images seen at the epicardial, endocardial and pericardial boundaries (Mulet-Parada and Noble 2000). For orientation selection, the appearance of bone surfaces was incorporated within our framework where a RT obtained from

the image ridgeness content measure was used to deduce the optimal angles of the directional filter. Because bone surfaces in US images typically appear as elongated line-like features, the RT that was used in this study is the classical RT where the integration of intensity values is performed along a line. This could be easily extended to a generalized RT where the integration could be performed on a curve that would be more suitable during enhancing circular features from US images.

Our qualitative and quantitative results on phantom, *in vivo* and clinical data demonstrate how the proposed technique for automatic filter parameter setting enables the robust capture of bone US image features based on local phase information, which is of great utility in US-based computer aided intervention systems.

Our future work will include the extension of automatic parameter selection to 3-D and the validation of the proposed method on other clinical scans that involve pelvic ring fractures.

REFERENCES

Amin DV, Kanade T, Digioia AM, Jaramaz B. Ultrasound registration of the bone surface for surgical navigation. J Comput Aided Surg 2003; 8:1–16.

Barratt DC, Penney PG, Chan SK, Slomczykowski M, Carter TJ, Edwards PJ, Hawkes DJ. Self-calibrating 3D-ultrasound-based bone registration for minimally invasive orthopaedic surgery. IEEE Trans Med Imaging 2006;25:312–323.

Barratt DC, Chan CSK, Edwards PJ, Penney PG, Slomczykowski M, Carter TJ, Hawkes DJ. Instantiation and registration of statistical shape models of the femur and pelvis using 3-D ultrasound imaging. Med Image Anal 2008;12:358–374.

Beek M, Abolmaesumi M, Luenam S, Ellis RE, Sellens RW, Pichora DR. Validation of a new surgical procedure for percutaneous scaphoid fixation using intraoperative ultrasound. Med Image Anal 2008;12:152–162.

Bosch JG, Mitchell SC, Lelieveldt BPF, Nijland F, Kamp O, Sonka M, Reiber JHC. Automatic segmentation of echocardiographic sequences by active appearance motion models. IEEE Trans Med Imaging 2002;21:1374–1383.

Boukerroui D, Noble JA, Robini M, Brady M. Enhancement of contrast regions in suboptimal ultrasound images with application to echocardiography. Ultrasound Med Biol 2001;27:1583–1594.

Brendel B, Winter S, Rick A, Stockheim M, Ermert H. Registration of 3-D CT and ultrasound datasets of the spine using bone structures. J Comput Aided Surg 2002;7:146–155.

Cao G, Shi P, Hu B. Ultrasonic liver discrimination using 2D phase congruency. IEEE Trans Biomed Eng 2006;53:2116–2119.

Coppola PT, Coppola M. Emergency department evaluation and treatment of pelvic fractures. Emerg Med Clin North Am 2000; 18:1–27.

Daanen V, Tonetti J, Troccaz J. A fully automated method for the delineation of osseous interface in ultrasound images. Proc MICCAI 2004. Lect Notes Comput Sci 2004;3216:549–557.

Frangi A, Niessen W, Vincken K, Viergever M. Multiscale vessel enhancement filtering. Proc MICCAI 1998. Lect Notes Comput Sci 1998;1496:130–137.

Foroughi P, Bocto E, Swatrz MJ, Taylor RH, Fichtinger G. Ultrasound bone segmentation using dynamic programming. IEEE Ultrason Symp 2007;2523–2526.

Grau V, Noble AJ. Adaptive multiscale ultrasound compounding using phase information. Proc MICCAI 2005. Lect Notes Comput Sci 2005;3749:589–596.

Hacihaliloglu I, Abugharbieh R, Hodgson AJ, Rohling RN. Enhancement of bone surface visualization from 3D ultrasound based on local phase information. Proc IEEE Ultrason Symp 2006;21–24.

Hacihaliloglu I, Abugharbieh R, Hodgson AJ, Rohling RN. Bone surface localization in ultrasound using image phase based features. Ultrasound Med Biol 2009a;35:1475–1487.

Hacihaliloglu I, Abugharbieh R, Hodgson AJ, Rohling RN. Automatic data-driven parameterization for phase based bone localization in US using Log-Gabor filters. Proc of 5th International Symposium on Visual Computing, Lecture Notes in Computer Science, 2009b; 5875:944–954.

Hanel DP, Jones MD, Trumble TE. Wrist fractures. Orthop Clin North Am 2002;33:35–57.

Ionescu G, Lavall'ee S, Demongeot J. Automated registration of ultrasound with CT images: Application to computer assisted prostate radiotherapy and orthopaedics. Proc of MICCAI 1999. Lect Notes Comput Sci 1999;1679:768–777.

Jain AK, Taylor RH. Understanding bone responses in B-mode ultrasound images and automatic bone surface extraction using a Bayesian probabilistic framework. Proc SPIE Med Imaging 2004;5733:131–142.

Kovesi P. Symmetry and asymmetry from local phase. Proc Tenth Australian Joint Conference on Artificial Intelligence 1997: 185–190.

Kowal J, Amstutz C, Langlotz F, Talib H, Ballester MG. Automated bone contour detection in ultrasound B-mode images for minimally invasive registration in computer assisted surgery an *in vitro* evaluation. Int J Med Robotics Comput Assisted Surg 2007;3:341–348.

Kryvanos A. Computer assisted surgery for fracture reduction and deformity correction of the pelvis and long bones. PhD thesis. University of Mannheim, Germany, 2002.

Lindeberg T. Edge detection and ridge detection with automatic scale selection. Int J Comput Vis 1998;30:117–154.

Madabhushi A, Metaxas DN. Combining low-, high-level andempirical domain knowledge for automated segmentation of ultrasonic breast lesions. IEEE Trans Med Imaging 2003;22:155–169.

McMurtry RY, Jupiter JB, Browner BD. Skeletal trauma: Fractures, dislocations, ligamentous-injuries. Saunders Publishing, 3rd edition, 2002.

Mulet-Parada M, Noble JA. 2D+T boundary detection in echocardiography. Med Image Anal 2000;4:21–30.

Pathak SD, Chalana V, Haynor DR, Kim Y. Edge-guided boundary delineation in prostate ultrasound images. IEEE Trans Med Imaging 2000;19:1211–1219.

Penney GP, Barratt DC, Chan CSK, Slomczykowski M, Carter TJ, Edwards PJ, Hawkes DJ. Cadaver validation of intensity-based ultrasound to CT registration. Med Image Anal 2006;10:385–395.

Phillips R. The accuracy of surgical navigation for orthopaedic surgery. Current Orthopaed 2007;21:180–192.

Sanchez-Ortiz G, Declerck J, Mulet-Parada M, Noble JA. Automatic 3D echocardiographic image analysis. Proc of MICCAI 2000. Lect Notes Comput Sci 2000;1935:687–696.

Smith WL, Fenster A. Optimum scan spacing for three-dimensional ultrasound by speckle statistics. Ultrasound Med Biol 2000;26:551–562.

Tonetti J, Carrat L, Blendea S, Merloz P, Troccaz J, Lavallee S, Chirossel JP. Clinical results of percutaneous pelvic surgery: Computer assisted surgery using ultrasound compared to standard fluoroscopy. J Comput Aided Surg 2001;6:204–211.

Wagner RF, Smith SW, Sandrik JM, Lopez H. Statistics of speckle in ultrasound B-Scans. IEEE Trans on Sonics and Ultrasonics 1983;30:156–163.

Ye X, Noble JA. 3-D freehand echocardiography for automatic left ventricle reconstruction and analysis based on multiple acoustic windows. IEEE Trans Med Imaging 2002;21:1051–1058.